

Structural transformation of carbon-encapsulated core-shell CoNi nanoparticles during magnetically induced CO₂ reduction into CO

Christian Cerezo-Navarrete^a, Irene Mustieles Marin^b, Carlo Marini^c, Bruno Chaudret^{b,*}, Luis M. Martínez-Prieto^{a,d,**}

^a ITQ, Institut de Tecnología Química, Universitat Politècnica de València (UPV), Av. de los Naranjos S/N, 46022, Valencia, Spain

^b LPCNO, Laboratoire de Physique et Chimie des Nano-Objets, UMR5215 INSA-CNRS UPS, Institut des Sciences appliquées, 135, Avenue de Rangueil, F-31077 Toulouse, France

^c ALBA Synchrotron Light Source, Barcelona, Spain

^d IIQ, Instituto de Investigaciones Químicas (CSIC-Universidad de Sevilla) – Departamento de Química Inorgánica, Avda. Americo Vespuco 49, 41092 Seville, Spain



ARTICLE INFO

Keywords:

Magnetically induced heating
Catalysis
CO₂ hydrogenation
Reverse water gas shift
Magnetic nanoparticles (MagNPs)

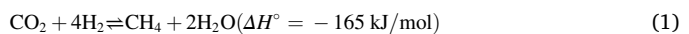
ABSTRACT

Controlling product distribution in CO₂ hydrogenation is of great scientific interest, the selective CO production through the reverse water-gas shift reaction (RWGS) being one of the most investigated processes. Herein, we report the synthesis of new core-shell Co@Ni NPs encapsulated in carbon (Co@Ni@C) to prevent their aggregation at the high-temperatures reached during magnetically induced catalysis. This bifunctional system has been simultaneously used as heating agent and catalyst for the magnetically induced hydrogenation of CO₂. While at low magnetic fields Co@Ni@C produces CH₄:CO mixtures, at higher field amplitudes it selectively generates carbon monoxide. Indeed, Co@Ni@C has shown to be one of the most active catalysts reported to date, which reaches a maximum conversion of 74.2% with complete selectivity towards CO at 53 mT and 300 kHz. In addition, recycling and cyclability experiments have demonstrated that Co@Ni@C becomes fully selective for CO after being exposed to high field amplitudes (*i.e.* reaction temperature above 500 °C), even when it exposed to low magnetic fields again. This change in the selectivity is due to an atomic rearrangement of the core-shell structure, as was confirmed by EDX, XAS, TPR and TPD analysis.

1. Introduction

The excessive production and release of greenhouse gases (GHS) leading to global warming is a worldwide problem, the main contributor being CO₂, and, as a result, its capture and subsequent use as feedstock or chemical reagent is one of the main present challenges for the scientific community [1]. In this respect, the hydrogenation of CO₂ to obtain highly valuable compounds is both of great scientific and applied interest. CO₂ can be reduced into methane through the Sabatier reaction (Eq. 1) [2], but another attractive way for reducing CO₂ is the Reverse Water-Gas Shift reaction (RWGS, Eq. 2) [3,4], which produces CO and H₂O [5–7]. The great versatility of CO as a C1 building block, as well as its use as a raw material for countless industrial processes [8], makes the RWGS an interesting option for the valorization of CO₂. RWGS is usually favoured at high temperatures due to its moderate endothermic

character and the high energy required for the activation of the CO₂ molecule [9,10]. At low temperatures (below 400 °C), RWGS is normally accompanied by the formation of CH₄ as a secondary product *via* CO₂ reduction [11,12], CO being the main product above 600–700 °C. Although this is one of the main limitations of the RWGS, it is already being exploited at an industrial level. Therefore, it is necessary to develop new catalytic processes that do not require large energy supplies to reach such working conditions [13].



Numerous catalysts based on supported metal nanoparticles (Pd, [14,15] Pt, [16,17] Fe, [18,19] Ni, [20,21] Cu, [22,23] etc.) have been reported to catalyze RWGS reaction. The use of supported-alloy metal

* Corresponding author.

** Corresponding author at: IIQ, Instituto de Investigaciones Químicas (CSIC-Universidad de Sevilla) – Departamento de Química Inorgánica, Avda. Americo Vespuco 49, 41092 Seville, Spain.

E-mail addresses: chaudret@insa-toulouse.fr (B. Chaudret), luismiguel.martinez@csic.es (L.M. Martínez-Prieto).

nanoparticles, such as Ni-Mo/γ-Al₂O₃, [24] Pd-In/SiO₂, [25] Cs-Cu/Mo₂C, [26] has also been studied for RWGS, leading to conversions between 20–50% with high selectivity towards CO (> 99%). One of the most active catalysts based on Ni (Ni/SiO₂) in RWGS was recently reported by Rossi *et al.* It shows good results in terms of conversion and selectivity (up to 70% conversion and 100% selectivity towards CO) [27, 28]. However, Ni/SiO₂ requires extremely high temperatures (~ 800 °C) to reach such conversions, which is accompanied by a substantial energy consumption. It is therefore necessary to explore novel reaction technologies that offer enhanced energy efficiency for selective CO₂ reduction to CO.

Magnetic induction heating by applying a high-frequency alternating magnetic field (AMF) has been known for a long time [29], and when considering nanoparticles, has found uses in biomedical applications such as cancer therapy (magnetic hyperthermia) [30]. Magnetic induction heating is based on the principle that ferromagnetic materials can produce heat by hysteresis losses when exposed to an AMF [31]. In this line, magnetic nanoparticles (MagNPs) have been successfully used to activate a multitude of catalytic reactions both in solution (e.g., hydrogenation, [32–35] amide condensation, [36–38] water splitting, [39, 40] hydrogenolysis [41]) and in the gas-phase (e.g., Fischer-Tropsch, [42] CO₂ hydrogenation, [43–46] methane reforming [47–49] or alkane dehydrogenation [50]), since they can simultaneously act as heating agents and catalysts. The heating power of MagNPs is commonly quantified by the specific absorption rate (SAR), which intimately depends on the physicochemical properties of the MagNPs (size, shape, composition, etc) [51,52]. The main advantage of magnetic heating is that it is a non-contact technique since the energy is directly transferred inside the ferromagnetic material to be heated, and thus displays the highest power transmission. This, together with its extremely short warming time, makes magnetically induced heating a very energetically efficient method and well-adapted to intermittent energy supply [31]. This is also why magnetic catalysis is a promising technology to carry out endothermic reactions that require high temperatures, such as RWGS.

On the other hand, understanding the function and location of active sites of heterogeneous catalysts in the same way that they can be determined in homogeneous systems is still a challenge. In most cases, the species active during catalysis are not found in the as-synthesized catalyst, due to atomic rearrangements that take place under reaction conditions [53,54]. That is why a multitude of analytical techniques such as HRTEM, EDX, XPS or XRD, have been efficiently employed for the determination of these active sites. In situ catalysts modifications can be due to diverse factors, such as change of crystal phase, [55] alteration of the particle size, [56] reactant-induced atomic displacement, [57] being one of the most observed atomic restructuration [58–60]. This type of structural reorganization usually occurs in multimetallic catalysts, where the migration of the atoms from the core to the surface of the nanoparticles and *vice versa* is observed. For example, in 1995 Bradley and coworkers observed a Pd-enrichment of the surface of bimetallic alloy-CuPd nanoparticles after exposing them to a CO atmosphere [61]. Years later, Somorjai *et al.* also reported how bimetallic nanoparticles of Rh_{0.5}Pd_{0.5} underwent a dynamic transformation in composition and chemical state as a function of the reaction atmosphere [62]. More recently, Liu and colleagues reported the atomic rearrangement of core-shell AuNi NPs during CO₂ hydrogenation. More specifically, they observed a reversible change in the core-shell structure at high-temperatures forming a transient reconstructed alloy surface promoted by the CO adsorption generated during the reaction [63]. Thus, the atomic rearrangement of the catalysts can be due to the affinity of the different metals for the reactants, [64] as well as the reaction conditions themselves [65].

Herein, we report an efficient magnetic catalyst based on core-shell Co@Ni nanoparticles encapsulated in carbon (Co@Ni@C). Similarly to our previous results, [66] the encapsulation in carbon prevents the sintering of MagNPs due to the high temperatures reached during the

catalysis. The synthesized catalyst has been fully characterized by state-of-the-art techniques, such as TEM, HRTEM, EDX, XPS, XAS, TPR and TPD measurements. Co@Ni@C has proven to be an exceptional catalyst for magnetically induced RWGS. In addition, we have found that Co@Ni@C undergoes a structural transformation under catalytic conditions, which is in between core-shell and pure alloy, making it highly active and selective for CO₂ hydrogenation to CO even at low field amplitudes (or low temperatures).

2. Experimental section

2.1. Synthesis of Co@Ni@C

This synthesis followed a three-step procedure. (i) First, the monometallic Co NPs were prepared according to previously reported procedure [66]. More specifically, Co precursor, [Co{N(SiMe₃)₂}₂·(THF)] (180 mg, 0.8 mmol), was reduced under 3 bar of H₂ upon heating at 150 °C for 24 h in mesitylene (20 mL) and in the presence of long chain surfactants, hexadecylamine (HDA; 386 mg, 1.6 mmol) and hexadecylamine hydrochloride (HDA-HCl; 333, 1.2 mmol). After reaction, a black solution with the magnetic Co NPs stabilized by HDA/HDA-HCl was obtained. (ii) In a second step, Ni(COD)₂ (220 mg, 0.8 mmol) was added to the Co NPs solution, and then reduced under 3 bar H₂ at 70 °C for 20 h. (iii) Once the Co@Ni NPs were formed, 920 mg of activated carbon (Norit D10) dispersed in 10 mL of mesitylene were added to the Fischer-Porter bottle that contains the suspension of Co@Ni NPs (92 mg). After vigorous stirring, Co@Ni NPs were adsorbed on the activated carbon. Then, carbon-supported Co@Ni NPs were washed with hexane three times, and dried at 60 °C overnight. The resulting black powder was then subjected to a pyrolysis process (2 h at 300 °C under N₂ pressure, with a heating ramp: 10 °C·min⁻¹), producing the Co@Ni NPs encapsulated in carbon (Co@Ni@C). The size of the carbon-coated NPs was measured by TEM for at least 100 nanoparticles, which afforded a mean value of 12.4 ± 2.8 nm (Fig. 2). ICP: Co: 5.1 wt %, and Ni: 5.3 wt%.

2.2. Synthesis of CoNi@C

The bimetallic CoNi alloy nanoparticles were synthesized through the simultaneous decomposition of the metal precursors [Co{N(SiMe₃)₂}₂·(THF)] (150.5 mg; 0.4 mmol) and Ni(COD)₂ (110.0 mg; 0.4 mmol) under 3 bar H₂ at 150 °C for 24 h in mesitylene (20 mL), in the presence of HDA (386.0 mg; 1.6 mmol) and HDA-HCl (333.5 mg; 1.2 mmol). After the reaction, a black solution containing the magnetic CoNi nanoparticles stabilized with HDA/HDA-HCl was obtained. The carbon encapsulation of these MagNPs was carried out in the same manner as described for Co@Ni@C. The size of the carbon-coated NPs was measured by TEM for at least 100 nanoparticles, which afforded a mean value of 9.3 ± 2.2 nm (see SI section S2, Fig. S13). ICP: Co: 4.4 wt %, and Ni: 4.9 wt%.

2.3. Digestion experiments

Following the procedure of Bao and co-workers, [67] who concluded that CoNi NPs were completely encapsulated in graphene because they were not soluble in a strong acid, we demonstrated that the carbon layer of Co@Ni@C and CoNi@C present a great number of cracks. Specifically, 10 mg of the sample were practically dissolved in a H₂SO₄ solution (2 M, 5 mL) at 80 °C after 2 h. Upon analyzing the resulting solutions by ICP-AES we observed a metal content of Co: 4.9 wt%, and Ni: 5.2 wt% for Co@Ni@C, and Co: 4.8 wt%, and Ni: 5.2 wt% for CoNi@C. This indicates that practically all metals present were dissolved due to the presence of a large number of gaps in the carbon layer. On the other hand, when the same digestion experiment was performed on Co@Ni@C pyrolyzed at 600 °C, the metal contents were Co: 3.9 wt%, and Ni: 4.1 wt%, which indicates a lower number of cracks or gaps in the

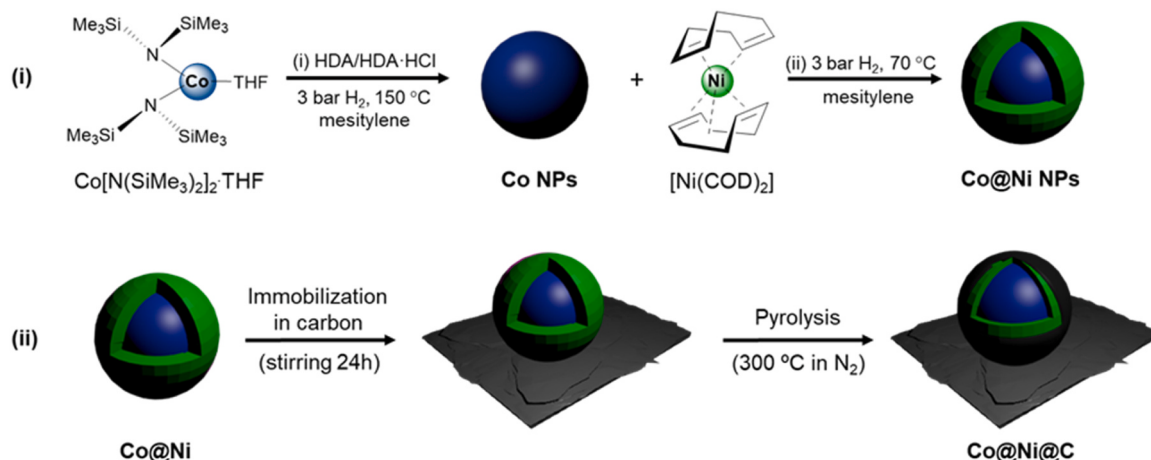


Fig. 1. Synthesis of Co@Ni@C following a two-step synthetic procedure: (i) generation of core-shell Co@Ni NPs by the controlled decomposition of Ni(COD)₂ on the surface of Co NPs and (ii) formation of Co@Ni@C by encapsulation of core-shell Co@Ni NPs on carbon through a pyrolysis process (2 h at 300 °C under a N₂ flow, 10 °C/min).

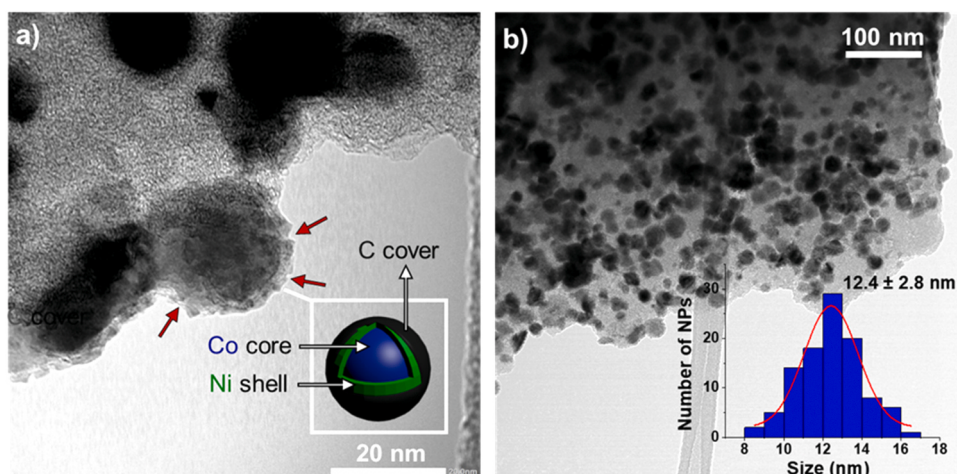


Fig. 2. (a, b) TEM micrographs and (b) size histogram of Co@Ni@C. The cracks of the carbon layer are highlighted by red arrows.

carbon layer.

2.4. Catalytic reactions

Catalytic experiments were performed in a quartz tube continuous-flow reactor of 1 cm inner tube diameter which was placed at the center of an inductor delivering an AC magnetic field oscillating at a frequency of 300 kHz with a root-mean-square (rms) amplitude adjustable between 0 and 65 mT (see SI section S2, Fig. S1). The cooper induction coil presents 2 no. of turns, and it is 3 cm wide and 2 cm high. The temperature was measured using an ultra-thin platinum thermocouple (TC Type K temperature probe with flexible measuring tip, short response time and 2 m cable) surrounded by quartz and located in the center of the catalytic bed. To avoid measurement errors, the response of the thermocouple was measured and corrected at different field amplitudes. Additionally, the local temperature (T_{bulk}) was verified using an infrared thermal camera, not observing differences in the temperature higher than 5 °C.

For a typical catalytic experiment, 400 mg of Co@Ni@C, CoNi@C or Co@C (2 cm height of catalytic bed) were used, supplying a flow rate of 25 mL·min⁻¹ with a CO₂:H₂ molar ratio of 1:4 (Pressure: 1 bar; GHSV: 70.7 L·h⁻¹·g⁻¹_{Ni}; 70750 mL·h⁻¹·g⁻¹_{Ni}).

In all cases, the outlet gases were injected into a GC-MS (Gas Chromatograph PerkinElmer 580 coupled to a Mass Spectrometer Clarus

SQ8T). Gas injection calibration and GC analysis method were performed using pure gases. The response factor of the analytes (RF_i = A_i/Concentration) was determined by injecting known quantities of each analyte *i* into the column. The area of the peak of species *i* in the chromatogram (A_i) allowed the determination of the conversion of *i* (X_i) and selectivity based on the following calculations.

$$X_{CO_2} = \frac{\sum A_{products,i} / RF_{products,i}}{\sum A_{products,i} / RF_{products,i} + A_{reactant,i} / RF_{reactant,i}} \quad (3)$$

$$Selectivity = \frac{A_{product,i} / RF_{product,i}}{\sum A_{products,i} / RF_{products,i}} \quad (4)$$

2.5. H₂-TPR connected to mass-spectrometer

In a typical experiment, 50 mg of Co@Ni@C after catalysis (Co@Ni@C_{after}) was heated from 25 to 450 °C at 5 °C/min under H₂ flow (10 vol% H₂ in Ar; 14 mL min⁻¹). The possible formation of CH₄ due to carbide hydrogenation was followed by online MS. During the entire experiment, the mass signals corresponding to an *m/z* = 16, 15 and 14 did not increase at all, indicating the absence of CH₄ species. Thus, this online experiment is not in agreement with the presence of nickel surface carbides in Co@Ni@C_{after}.

2.6. Regeneration experiment

For this regeneration experiment, 400 mg of $\text{Co@Ni@C}_{\text{after}}$ was placed into a quartz tube continuous-flow reactor. While heating to 500 °C, a H_2 stream (25 $\text{mL}\cdot\text{min}^{-1}$) was flowed through the catalyst during 5 h with the aim of removing any pollutants or nickel carbide species formed during the magnetic catalysis. After this regeneration treatment, $\text{Co@Ni@C}_{\text{after}}$ was used as catalysts under magnetic heating and the standard reaction conditions (25 mL min^{-1} , $\text{CO}_2:\text{H}_2$ 1:4 molar ratio at different field amplitudes), observing that the catalyst keeps the selective towards CO at low magnetic fields/temperatures.

3. Results and discussion

3.1. Synthesis and characterization

Core-shell Co@Ni NPs encapsulated in carbon (Co@Ni@C) were synthesized according to the synthetic procedure described in Section 2.1 (Fig. 1), which is based in a previously reported method [35,66]. The carbon encapsulation of Co@Ni NPs is important to prevent their sintering when exposed to the high temperatures reached during the magnetically induced catalysis. However, it is key to carry out the encapsulation process at 300 °C for two reasons: (i) to keep the core-shell structure of the carbon-coated Co@Ni NPs, since at higher pyrolysis temperatures these MagNPs become alloyed, and (ii) to form a cracked carbon layer with a large number of gaps that allow the access of substrates to the active metal surface. The metal content of Co@Ni@C was determined by inductively coupled plasma atomic emission spectroscopy (ICP-AES), using an already reported digestion method [67, 68]. In detail, Co@Ni@C has a total metal content of 10.4 wt% (Co: 5.1 wt%, and Ni: 5.3 wt%), corresponding to a NP composition of $\text{Co}_{49}:\text{Ni}_{51}$, which is very close to the theoretical value ($\text{Co}_{50}:\text{Ni}_{50}$).

TEM images of Co NPs before the formation of the Ni shell show spherical and well-distributed nanoparticles with a mean size of 10.1 ± 1.9 nm (see SI section S3, Fig. S2). After the controlled decomposition of the Ni precursor, uniform core-shell Co@Ni NPs were obtained with a slightly larger size due to the incorporation of the Ni layer (11.1 ± 2.5 nm) (see SI section S3, Fig. S3). Finally, after the encapsulation into carbon, the NP size slightly increases to 12.4 ± 2.8 nm, due to a minor sintering of the MagNPs during the pyrolysis process (Fig. 2).

The crystallinity and metallic composition of Co@Ni@C were studied by high-resolution TEM (HRTEM) and scanning transmission electron microscopy (STEM) using a high-angle annular dark-field detector (HAADF) coupled to Energy-dispersive X-ray (EDX) spectroscopy.

HRTEM images of Co@Ni@C show crystalline core-shell NPs, with a *fcc* (face-centered cubic) cobalt core and a *fcc* nickel shell (Fig. 3a). In addition, it was observed by HRTEM that these crystalline NPs are covered with a cracked carbon coat of *ca.* ~ 3 nm (Fig. 3b). Despite the large number of cracks observed in this carbon layer, it prevents the sintering of Co@Ni NPs at the high temperatures reached during the magnetic catalysis (*vide infra*). The presence of these cracks was confirmed by a simple digestion experiment, where carbon-encapsulated Co@Ni NPs were totally disaggregated using a H_2SO_4 solution (10.1 wt% of metal content, calculated by ICP-AES). This large number of gaps is due to the incomplete encapsulation of MagNPs when the pyrolysis is carried out at 300 °C. The chemical order was studied by STEM-HAADF coupled with EDX analysis. The EDX line scan profile of Co@Ni@C shows core-shell NPs coated by a carbon layer with an atomic composition of $\text{Co}_{47}:\text{Ni}_{53}$ (Fig. 3c), which is very close to the ICP results (*vide supra*) and matches very well the theoretical composition ($\text{Co}_{50}:\text{Ni}_{50}$). Note that, as mentioned before, the encapsulation temperature is critical since, for example, at 600 °C core-shell Co@Ni NPs undergo a complete atomic restructuration, where surface Ni atoms diffuse into the core of the nanoparticle forming alloy-type NPs (see SI section S4, Fig. S5).

A Raman spectrum of Co@Ni@C (see SI section S5, Fig. S8) shows two major peaks at 1348 cm^{-1} and 1606 cm^{-1} , associated to bands D and G respectively, which are characteristic of carbon based materials [69]. The high intensity of the D band is in turn associated with the presence of a large number of defects in this carbon material.

The X-Ray diffractogram of Co@Ni@C exhibits a series of low intensity peaks corresponding to *fcc*-Co and *fcc*-Ni together with peaks attributed to CoO and NiO , confirming the partial oxidation of the MagNPs encapsulated in the cracked carbon layer after air exposure (see SI section S6, Fig. S9).

The chemical composition and oxidation states of Co@Ni@C NPs were investigated by X-ray photoelectron spectroscopy (XPS). Fig. 4a shows the Ni 2p and Co 2p areas of these carbon-encapsulated Co@Ni NPs. The Ni 2p area presents a main peak at 855.1 eV, which can be deconvoluted into two components: (i) a major contribution at 855.5 eV that corresponds to Ni oxide (NiO) and (ii) a minor one at 853.0 eV belonging to metallic Ni (Ni^0). In the same way, the Co 2p region exhibits a strong emission at 780.3 eV, which after deconvolution displays two bands, a big one at 780.9 eV corresponding to Co oxide (CoO) and a small one at 778.9 eV of Co^0 . Therefore, by analysing Ni 2p and Co 2p XPS regions, we can deduce that the surface of as-synthesized Co@Ni@C NPs are mostly oxidized due to their purification under air. Remarkably, after catalysis under reductive conditions Co@Ni@C are

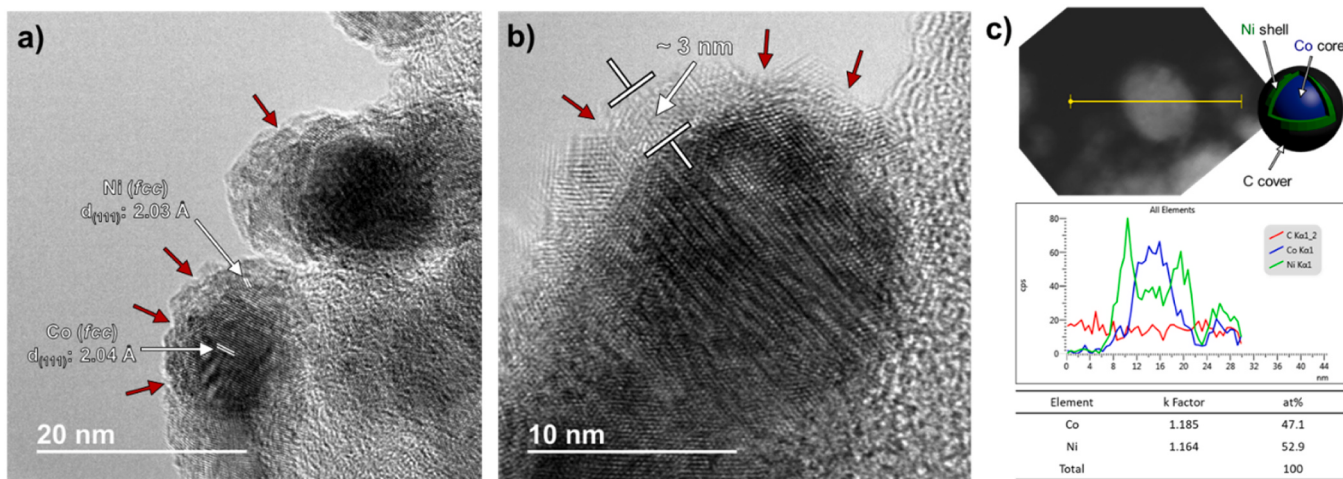


Fig. 3. HRTEM micrographs of Co@Ni@C . (a) Lattice spacings of *fcc* Co (2.04 Å) and Ni Co (2.03 Å) are highlighted in white. (b) Thickness of the carbon coat (~ 3 nm). The cracks of the carbon layer are highlighted by red arrows. (c) STEM-HAADF image, EDX line scan profile and Co:Ni ratio (at%) of Co@Ni@C .

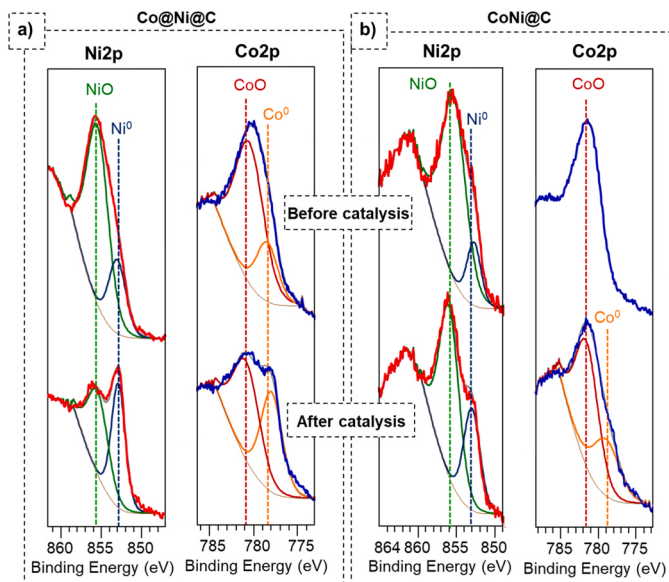


Fig. 4. X-ray photoelectron spectroscopy (XPS) of Ni 2p and Co 2p areas of (a) Co@Ni@C and (b) CoNi@C before (top) and after (bottom) catalysis.

partially reduced (*vide infra*).

The magnetic properties of **Co@Ni@C** NPs were measured by Vibrating Sample Magnetometry (VSM) applying a magnetic field between - 3 and 3 T at 300 K and 5 K. The obtained hysteresis loops provide the corresponding saturation magnetization (M_S) and coercive field (H_C) values for **Co@Ni@C** (see SI section S7, Fig. S11a). The M_S obtained are $65 \text{ A}\cdot\text{m}^2\cdot\text{g}^{-1}$ at 300 K and $70 \text{ A}\cdot\text{m}^2\cdot\text{g}^{-1}$ at 5 K, which are considerably lower than that reported for the same cobalt NPs encapsulated in carbon (**Co@C**; M_S of $120\text{--}130 \text{ A}\cdot\text{m}^2\cdot\text{g}^{-1}$) due to the incorporation of the Ni shell [35]. The existence of a perceptible *exchange bias* field in the hysteresis loops (shifted along $\mu_0 H_C$ axis) confirms the partial oxidation of **Co@Ni@C** (see SI section S7, Fig. S11b).

The heating capacity of **Co@Ni@C** NPs was evaluated by determining their specific absorption rate (SAR) by calorimetry using a previously reported procedure (see SI, section S8) [42,43,70]. The SAR values at different field amplitudes (from 0 to 47 mT) were determined in the solid state after the application of an alternating magnetic field ($\mu_0 H_{rms}$) with a frequency of 93 kHz (see SI section S8, Fig. S15). **Co@Ni@C** starts to heat up at 19 mT, reaching a maximum SAR value of 76 W·g⁻¹ at 47 mT. This value is slightly lower than the one obtained for the analogous reported material based on carbon-encapsulated cobalt NPs (**Co@C**; 120 W·g⁻¹), due to the presence of the nickel-shell which is a magnetically softer material. Although these SAR values are somewhat low, they have proven to be enough to reach very high temperatures under high frequency AMFs [66].

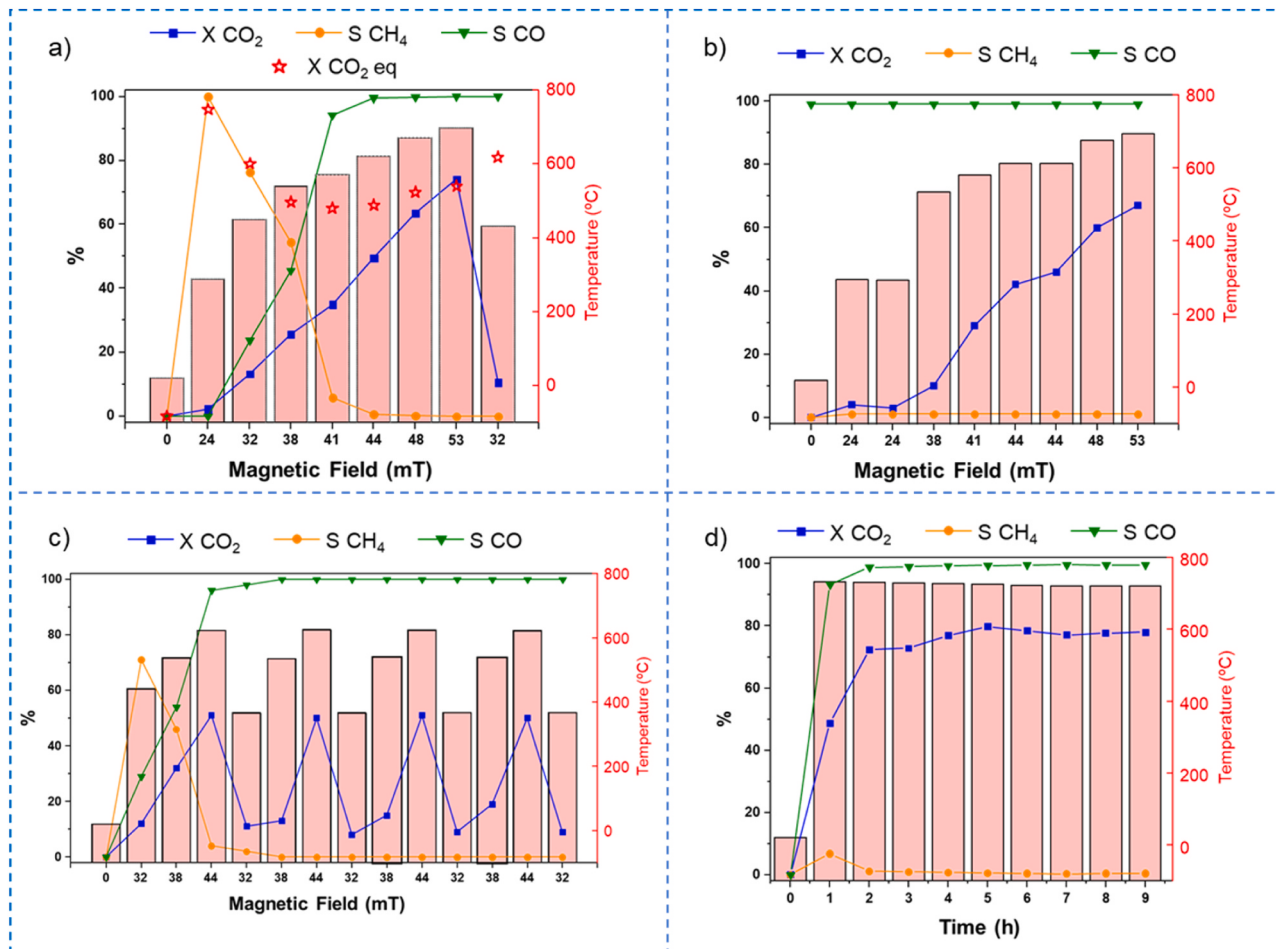


Fig. 5. Magnetically induced CO₂ hydrogenation reaction using (a) Co@Ni@C and (b) Co@Ni@C_{after}. (c) Cyclability study of magnetically induced CO₂ hydrogenation reaction using Co@Ni@C. (d) Catalytic performances of Co@Ni@C over time. Gas flow: 25 mL min⁻¹ CO₂:H₂ (1:4) (GHSV = 70750 mL·h⁻¹ g_{Ni}⁻¹). X = conversion and S = selectivity. Equilibrium conversion of CO₂ at different temperatures are represented by red stars. Temperatures (red bars) were recorded by an ultrathin thermocouple directly located in the catalytic bed and confirmed by IR thermometry.

3.2. Catalytic studies

Co@Ni@C was simultaneously used as heating agent and catalyst in continuous flow magnetically induced CO₂ hydrogenation, employing a gas feed of CO₂:H₂ mixture with a 1:4 molar ratio (5 mL·min⁻¹ CO₂ and 20 mL·min⁻¹ of H₂). At low field amplitudes (from 24 to 38 mT), the conversions are low (< 25%), producing mixtures of methane and CO (Fig. 5a). For example, at 32 mT the conversion is only 13.2% with 76% selectivity towards CH₄ and 24% to CO. However, at 41 mT **Co@Ni@C** begins to selectively convert CO₂ into CO (34.9% of conversion with 94% selectivity to CO). At 44 mT, the selectivity towards CO is 100% with a conversion of 49.5%. Increasing the field amplitude led to higher conversions keeping the high selectivity toward CO, which reaches a maximum conversion value of 74.2% at 53 mT. The bulk temperature (T_{bulk}) of the system, determined by an ultrathin thermocouple located in the middle of the catalytic bed, also increases with the field amplitude from 289 °C at 24 mT to 698 °C at 53 mT. Remarkably, the conversion at 53 mT (T_{bulk} = 698 °C) is slightly higher than the expected conversion at the thermodynamic equilibrium at the estimated temperature (~ 70%; Table 1, entry 1 and Fig. S16), which suggests that surface temperature (T_{surf}) of **Co@Ni@C** is above the measured T_{bulk} value, as was previously observed in similar systems [35,71]. According to the conversion observed at 53 mT (74.2%), it can be estimated that the catalyst surface is above 750 °C (see SI section S9, Fig. S16). In comparison to the catalytic systems already reported in the literature, **Co@Ni@C** seems to be one of the most active catalysts in the selective hydrogenation of CO₂ to CO (RWGS) (see SI section S10, Table S1). Finally, after decreasing the field amplitude to 32 mT, the high selectivity to CO observed at high temperatures is retained, leading to 10.5% of CO₂ conversion with 100% selectivity towards CO. The later result indicates that the change observed in the selectivity is not only a matter of temperature (normally in CO₂ hydrogenation the RWGS is favoured at high temperatures and Sabatier reaction at lower ones). Thus, this change in the selectivity of **Co@Ni@C** NPs must be due to a structural transformation of the catalyst and/or the formation of new actives sites during the magnetically induced catalysis, since both the nanoparticle size and morphology remain practically unchanged as can be observed by TEM images after catalysis (see SI section S3, Fig. S4).

To confirm the change observed in the selectivity of **Co@Ni@C**, recyclability and cyclability experiments were carried out. First, the same continuous flow catalytic test was performed with an already used and recovered **Co@Ni@C** catalyst (**Co@Ni@C_{after}**). As shown on Fig. 5b, the selectivity toward CO is 100% even at low field amplitudes and conversions, which indicates that the catalyst becomes selective during the first catalytic cycle. Here, the conversion also increases linearly in all the range of magnetic field amplitudes, reaching a 67% of conversion of CO₂ at 53 mT, which is slightly lower than the value obtained with fresh **Co@Ni@C** catalyst (Fig. 5a). This may be due to a higher degree of encapsulation of the MagNPs when reaching temperatures above 600 °C during the first catalytic cycle, which would reduce the number of available active sites. Secondly, a cyclability experiment at variable field amplitudes (from 32 to 44 mT) was also performed for **Co@Ni@C**. More specifically, conversions and selectivities at 32, 38 and 44 mT were measured cyclically (Fig. 5c). Remarkably, **Co@Ni@C** exhibits almost perfect cyclability in terms of temperature (620 °C) and CO₂ conversion (~ 50%). Regarding selectivity, at low field amplitudes (i.e. 32 mT), the conversion is low (12%) and the reaction products are a CH₄:CO mixture, methane being the major product (71% selectivity). After increasing the magnetic field to 38 mT, the conversion increases to 32% but the selectivity changes, CO being the main product (54% selectivity). A drastic change in selectivity occurs when a certain T_{bulk} value is reached (> 500 °C), leading exclusively to CO as the main reaction product. Accordingly, the change in the selectivity of **Co@Ni@C** occurs when this temperature is reached, since by decreasing the field to the initial values (32 mT) the formation of methane is no longer observed. In addition, **Co@Ni@C** has been shown to be stable for at least

9 h under reaction conditions, without showing any significant loss in activity or selectivity (~ 75% conversion and > 99% selectivity to CO after 9 h of reaction; Fig. 5d). Therefore, we can conclude that the carbon coat significantly increases the stability of these MagNPs, avoiding their agglomeration and allowing them to maintain both their activity and heating capacity during long reaction periods.

As previously mentioned, the encapsulation of **Co@Ni** NPs was carried out at 300 °C, since at higher temperatures (i.e. 600 °C) the core-shell structure undergoes an atomic rearrangement where Ni atoms diffuse from the shell towards the nanoparticle nucleus, forming alloy-type nanoparticles (see SI section S4, Fig. S5). In a similar way, during the catalysis at field amplitudes higher than 44 mT (above 500 °C), an irreversible structural transformation occurs in the MagNPs, forming alloy-type CoNi nanoparticles. This structural change was confirmed by STEM-EDX analysis of **Co@Ni@C_{after}**, where diverse types of MagNPs can be observed with different degrees of atomic arrangements: core-shell like, alloy type and intermediate states between alloy and core-shell (Fig. 6). Possibly, the change in selectivity observed during the catalysis is due to the atomic rearrangement that **Co@Ni@C** undergoes under high field amplitudes, resulting in an intermediate state between core-shell and alloy. This gradient of concentration of one metal into the other led to a modification of the magnetic anisotropy and hence of the heating power as was observed by VSM measurements (higher values of M_s and H_C; see SI section S7, Fig. S12).

Once observed that the atomic rearrangement in **Co@Ni@C** that takes place during the magnetic catalysis, where most of the MagNPs evolve from core-shell to alloy, we proceeded to synthesize the analogous alloy type material (**CoNi@C**) and test it in the same catalytic reaction. More specifically, the alloy-type CoNi NPs were prepared following a co-decomposition of Co and Ni precursors, which were subsequently encapsulated in carbon by a pyrolysis process as described in Section 2.2. The metallic content of **CoNi@C** is very close to the theoretical value, presenting 4.4 wt% Co and 4.9 wt% Ni. In addition, by TEM and STEM-EDX analysis it was possible to confirm that these MagNPs were alloy type and display a particle size of 9.3 ± 2.2 nm (see SI section S4, Fig. S6), very similar to the size observed for the core-shell type catalyst (**Co@Ni@C**).

After the characterization of the surface of **CoNi@C** by XPS (see Fig. 4b), and Raman (see SI section S5, Fig. S8), it was observed that Co is mostly oxidized because cobalt atoms are more exposed to air in these alloy-type NPs. For example, unlike **Co@Ni@C** Raman spectrum, that of **CoNi@C** shows small peaks which can be attributed to Co-O (207 and 464 cm⁻¹) [72,73]. Then, **CoNi@C** was tested in the magnetic hydrogenation of CO₂ (Fig. 7) under the catalytic conditions previously described (gas flow: 25 mL min⁻¹, molar ratio CO₂:H₂ 1:4). In the same way as **Co@Ni@C**, at low field amplitudes (32 mT) **CoNi@C** produces CO:CH₄ mixtures, the main product being methane (7.3% conversion and 58.5% selectivity to CH₄). However, at field amplitudes higher than 44 mT, CO becomes the only reaction product. At 53 mT (maximum field amplitude applied) the yield of CO is 51.3% (T_{local} = 646 °C). Similarly to **Co@Ni@C**, if we decrease the magnetic field applied again to 32 mT, the selectivity to CO is maintained, even at low T_{bulk} and conversion (~ 400 °C and 5.8% conversion). Although **CoNi@C** presents a very similar catalytic behavior to **Co@Ni@C**, this catalyst is less active. At the same field amplitude value (53 mT), the alloy-type catalyst reaches a maximum conversion of 51.3%, while **Co@Ni@C** shows a conversion of 74.2%. This difference in activity is probably due to the higher bulk temperature reached with the core-shell catalyst at 53 mT (T_{bulk} of 698 °C), since with **CoNi@C** the T_{bulk} is only 646 °C, which is attributed to the lower magnetic properties (M_s and H_C) of **CoNi@C** (see SI section S7, Fig. S13). However, after comparing the catalytic performance of **Co@Ni@C** and **CoNi@C** at the same bulk temperature (i.e. T_{bulk} ~ 625 °C), the activity of **Co@Ni@C** is slightly higher (conversion of 49.5% at T_{bulk} = 622 °C and 44 mT) to that of **CoNi@C** (conversion of 42.2% at T_{bulk} = 629 °C and 48 mT), indicating that the higher activity of **Co@Ni@C** cannot be only attributed to its superior magnetic

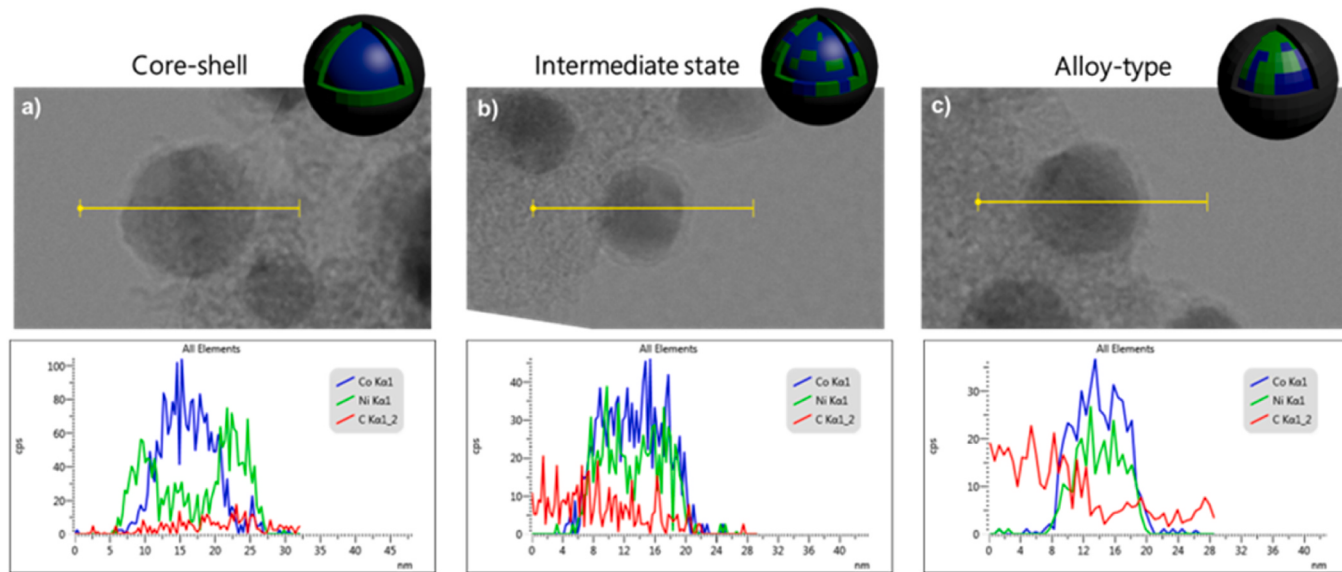


Fig. 6. STEM-BF images and their corresponding EDX line scan profiles of $\text{Co@Ni@C}_{\text{after}}$ at different atomic arrangements.

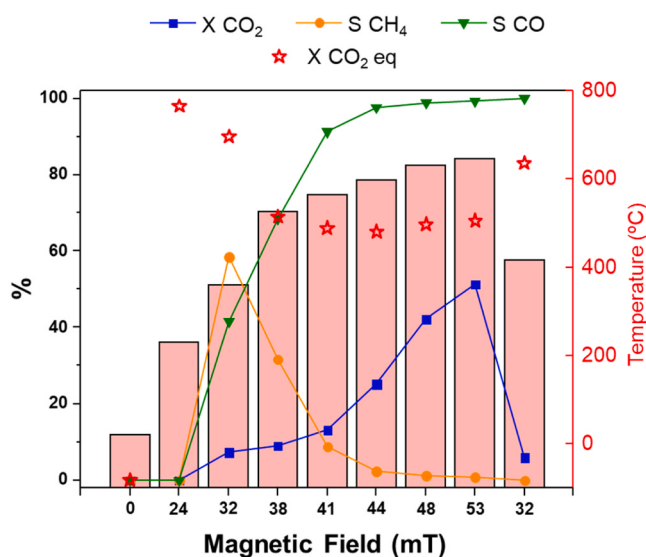


Fig. 7. Magnetically induced CO_2 hydrogenation reaction using CoNi@C . Gas flow: $25 \text{ mL min}^{-1} \text{ CO}_2:\text{H}_2$ (1:4) ($\text{GHSV} = 1500 \text{ h}^{-1}$). X = conversion and S = selectivity. Equilibrium conversion of CO_2 at different temperatures are represented by red stars. Temperatures (red bars) were recorded by an ultrathin thermocouple directly located in the catalytic bed and confirmed by IR thermometry.

properties. The cyclability studies of CoNi@C revealed a similar behavior to that previously observed for Co@Ni@C (see SI section S11, Fig. S17), but with less activity. In the first cycle, at low field amplitudes (i.e. 32 mT) the conversion is 6.3% with 63% selectivity towards methane. However, when the field is increased to 44 mT only CO is obtained (18.2% conversion and >99% selectivity). After performing successive 32–38–44 mT cycles, methane formation is no longer observed. The latter results show that in the same way than for Co@Ni@C , at a certain local temperature (> 500 °C) a change in selectivity takes place, with CO being the only product of the reaction. A comparative VSM analysis of CoNi@C before (Fig. S13) and after catalysis (Fig. S14), also indicates a significant modification of the magnetic properties (higher M_s and H_c values) under catalytic conditions.

To confirm that high temperatures (> 500 °C) are responsible for the atomic restructuration and the change in the selectivity observed in Co@Ni@C during the catalysis, we proceeded to perform the hydrogenation of CO_2 under conventional heating and the standard reaction conditions (25 mL min^{-1} , $\text{CO}_2:\text{H}_2$ 1:4 molar ratio) with fresh Co@Ni@C (see SI section S11, Fig. S18). The conversions are significantly lower over the entire temperature range. For example, at 400 °C the conversion is only 5.3% with 57.9% selectivity towards CH_4 and 42.1% to CO. As temperature increases, the conversion increases too and the selectivity shifts towards CO, reaching a maximum conversion of 16.6% at 600 °C (maximum operation temperature of the conventional heating reactor) and a selectivity to CO of 99%. Comparing the latter result with that obtained by magnetic induction at similar T_{bulk} (i.e. T_{bulk} of 620 °C at 44 mT), we observe a much higher conversion when the catalyst is magnetically heated (conversion of 16.6% vs. 49.5%). As was previously observed, under an oscillating magnetic field the surface temperature of the catalyst (T_{surf}) is much higher than the measured T_{bulk} , which is normally reflected in higher conversions at the same T_{bulk} . In terms of selectivity, under conventional heating Co@Ni@C shows the same behaviour as a magnetically heated sample. It maintains the high selectivity towards the formation of CO even after reducing again the temperature (6.8% conversion with 100% selectivity towards CO at 400 °C) (see SI section S11, Fig. S18). STEM-EDX analysis of Co@Ni@C after conventional heating indicates a similar structural transformation to the one previously observed after magnetic catalysis (see SI section S4, Fig. S7). Thus, we can propose that the structural transformation that produces the change in the selectivity of the catalyst is caused by the temperature reached during the catalytic reaction.

In order to determine the role of Co in the reactivity of these catalysts, the analogous monometallic material was prepared (Co@C , [66]) and tested in the magnetically induced CO_2 hydrogenation (see SI section S11, Fig. S19a). In summary, when Co@C was used as a catalyst under the standard reaction conditions (25 mL min^{-1} , $\text{CO}_2:\text{H}_2$ 1:4 molar ratio), at low field amplitude (32 mT) the conversion is very low (1.8%) and produces mixtures of $\text{CH}_4:\text{CO}$ (53.7% selectivity towards CH_4). As the field amplitude increases, the conversion and selectivity towards CO increase, reaching a maximum conversion at 53 mT with high selectivity towards CO (44.3% of conversion with 97% selectivity; $T_{\text{bulk}} = 635$ °C). However, unlike the bimetallic catalysts (Co@Ni@C and CoNi@C), when low field amplitudes are again applied (i.e. 32 or 24 mT) mixtures of $\text{CO}:\text{CH}_4$ are observed (see SI section S11, Fig. S19a). This latter result indicates that the presence of Ni not only increases the activity of these

catalysts, but also significantly improves their selectivity to CO after being exposed to high magnetic fields. This behavior was corroborated by a cyclability study (see SI section S11, Fig. S19b). Contrary to bimetallic catalysts, **Co@C** follows the same pattern during the successive cycles; CH₄:CO mixtures are produced at low magnetic fields and CO at high fields. Therefore, we can confirm that **Co@C** does not suffer any change in the selectivity after exposing it to high magnetic fields. In addition, we can assume that if any Co carbide species are formed during the magnetic catalysis at high temperatures, they are not responsible for the change in the selectivity observed for the CoNi bimetallic systems. On the other hand, since the formation of Ni carbide species may be responsible for this change in selectivity towards CO, as was recently reported, [27] we decided to better analyze **Co@Ni@C_{after}** looking for Ni-C species. Neither by direct (XRD, XPS or XAS) nor indirect techniques (H₂-TPR connected to a MS to probe methane formation [74] and testing of catalytic activity after a regeneration treatment; [75] see Experimental section, sections S1) were able to demonstrate the presence of Ni carbides. Thus, the change in selectivity should be due to the atomic restructuration observed at high magnetic fields/temperatures.

In summary, as can be seen in Table 1, core-shell MagNPs (**Co@Ni@C**) present the highest activity in the selective hydrogenation of CO₂ to CO, being one of the most active catalysts reported to date (see SI section S10, Table S1). The lower activity of the alloy-type catalyst (**CoNi@C**) indicates that, even when an atomic rearrangement occurs on **Co@Ni@C** NPs during magnetic catalysis, they do not form a perfect alloy but remain in an intermediate state which favors their heating capacity and activity in the selective reduction of CO₂ to CO. A similar behavior was previously observed in bimetallic FeCo NPs, where their magnetic properties and heating capacities were highly dependent on their internal structures [76]. On the other hand, the selectivity change observed during the magnetic catalysis with bimetallic catalysts (**Co@Ni@C** and **CoNi@C**), suggests that these catalysts can also undergo some type of structural transformation that make them selective towards CO.

3.3. Structural transformation studies

With the intention of studying the change in selectivity of **Co@Ni@C** and **CoNi@C** during the magnetically induced catalysis at high field amplitudes, the local environment of these bimetallic catalysts before and after catalysis was examined by X-ray absorption spectroscopy (XAS) experiments (XANES and EXAFS). In this way it was possible to study in depth the oxidation state and coordination number of metal centers of these heterogeneous catalysts. The normalized XANES spectra at the Co-K and Ni-K edges of the bimetallic catalysts before (**Co@Ni@C** and **CoNi@C**) and after catalytic conditions (**Co@Ni@C_{after}** and **CoNi@C_{after}**) can be observed in Fig. 8a-b. When comparing the XANES spectra of the bimetallic samples with the Co and Ni references, we can observe that in all samples both Co and Ni are present mainly as zerovalent metals (Table 2). This observation is not in agreement with the results previously observed by XPS (see Fig. 4), where it was seen that MagNPs were mostly oxidized before applying reducing conditions. However, XPS is a surface characterization technique, and it is only

capable of determining the oxidation states of atoms located in the outer layers, which are more exposed to air. On the other hand, in line with XPS data, **Co@Ni@C_{after}** is more reduced than the as-synthesized catalyst. More specifically, before catalysis, 89.5% of the cobalt is found as Co⁰ and 81.2% of the nickel is as Ni⁰, while after catalysis, 93.9% of the cobalt and 92.8% of the nickel are found in their respective zerovalent states (Table 2, entries 1 and 2). Under reductive reaction conditions (25 mL min⁻¹ of CO₂:H₂ 1:4) and magnetic induction heating, the small fraction of metal oxides present on the catalyst surface is mostly reduced. This was confirmed by “*in-situ*” XRD analysis at different temperatures (r.t., 100, 200, 300, 400, 500 and 600 °C) under reaction conditions (see SI section S6, Fig. S10). Under reaction conditions, the small peaks attributed to oxidized Ni and Co species disappear as the temperature rises, while the peaks associated to the reduced species (fcc-Co and fcc-Ni) increase, in agreement with XANES observations. In the case of the alloy-type catalyst (**CoNi@C**) a similar trend is observed for cobalt, which is reduced under reaction conditions (from 67.8% to 82.0%; Table 2, entries 3 and 4). The higher amount of CoO in **CoNi@C** than in **Co@Ni@C** is due to the fact that Co is more exposed to air in alloy-type MagNPs. In the core-shell catalyst (**Co@Ni@C**), the Ni shell acts as a protective layer against the oxidation of the Co core. However, in the case of nickel we can observe that **CoNi@C_{after}** presents a higher proportion of NiO than **CoNi@C** (9.0% and 23.5%, respectively; entries 3 and 4). This can be related to an enrichment in Ni of the NP surface after catalytic conditions, where without forming a core-shell NP it approaches to the mentioned intermediate state that makes the catalyst completely selective to CO even at low magnetic fields. Thus, the higher oxidation degree of Ni in **CoNi@C_{after}** can be explained by a greater number of Ni atoms on the NP surface after catalysis.

To shed some light about the local structure of the intermediate state between core-shell and alloy observed in bimetallic systems after catalysis, EXAFS spectroscopy analysis of **Co@Ni@C** and **CoNi@C** before and after catalytic conditions was performed. EXAFS data of these samples together with metallic foils and their oxides are shown in Fig. 8c-d (see also Fig. S20, section S12). EXAFS data shows that Ni atomic centers in the first coordination shell of **Co@Ni@C** were coordinated to other metal with a coordination number (N) of 6.81, due to its core-shell structure (Table 3, entry 1). On the other hand, after catalytic conditions this coordination number increases up to 9.24 (Table 3, entry 2), confirming that Ni atoms were diffused into the Co core during magnetic catalysis, as was previously observed by EDX. However, **Co@Ni@C_{after}** does not present a perfect alloyed structure, since it exhibits a number of neighboring atoms (N) different from that observed for the alloy type catalyst, **CoNi@C** (Table 3, entry 3). Moreover, after comparing **Co@Ni@C_{after}** and **CoNi@C_{after}** they show very similar Co-M and Ni-M values, suggesting that an atomic restructuration where one metal diffuse into the other takes place on both catalysts, since they present similar local environments (Table 3, entries 2 and 4). Therefore, from XANES and EXAFS data it has been possible to confirm the existence of an intermediate state between core-shell and pure alloy. This concentration gradient is produced as a consequence of an atomic rearrangement of the MagNPs under catalytic conditions at high reaction temperatures (> 500 °C) and turns the catalysts highly selective towards CO even at low field amplitudes.

Finally, TPR (temperature-programmed reduction) and TPD (temperature-programmed desorption) of CO and CO₂ experiments were carried out in order to investigate the high selectivity towards the CO formation of **Co@Ni@C_{after}** and **CoNi@C_{after}** catalysts. First, the reducibility of the different catalysts, **Co@Ni@C**, **CoNi@C** and **Co@C**, was compared (see Fig. 9 and S21 of SI section S13). The TPR profile of the monometallic catalyst **Co@C** shows a reduction peak at ~320 °C (Fig. S21). On the other hand, the reduction of CoO in the bimetallic catalysts observed in their TPR profiles takes place at lower temperatures, which is due the presence of Ni (Fig. 9), as previously reported [77,78]. More specifically, **Co@Ni@C** exhibits two reduction peaks at 168 and 232 °C, which are attributed to the reduction of CoO and NiO

Table 1
Magnetically induced CO₂ hydrogenation using **Co@Ni@C**, **CoNi@C** and **Co@C** as catalysts.

Catalyst	Conversion (%)	Selectivity (%)	T _{bulk} (°C) ^a	Conversion at thermodynamic Eq. (%) ^b
Co@Ni@C	74.2	> 99	698	72
CoNi@C	51.3	> 99	646	68
Co@C	44.3	97	635	67

^a T_{bulk} was recorded by an ultrathin thermocouple directly located in the catalytic bed. ^bConversions at thermodynamic equilibrium were estimated employing the Gibbs free energy minimization method and are based on T_{bulk}.

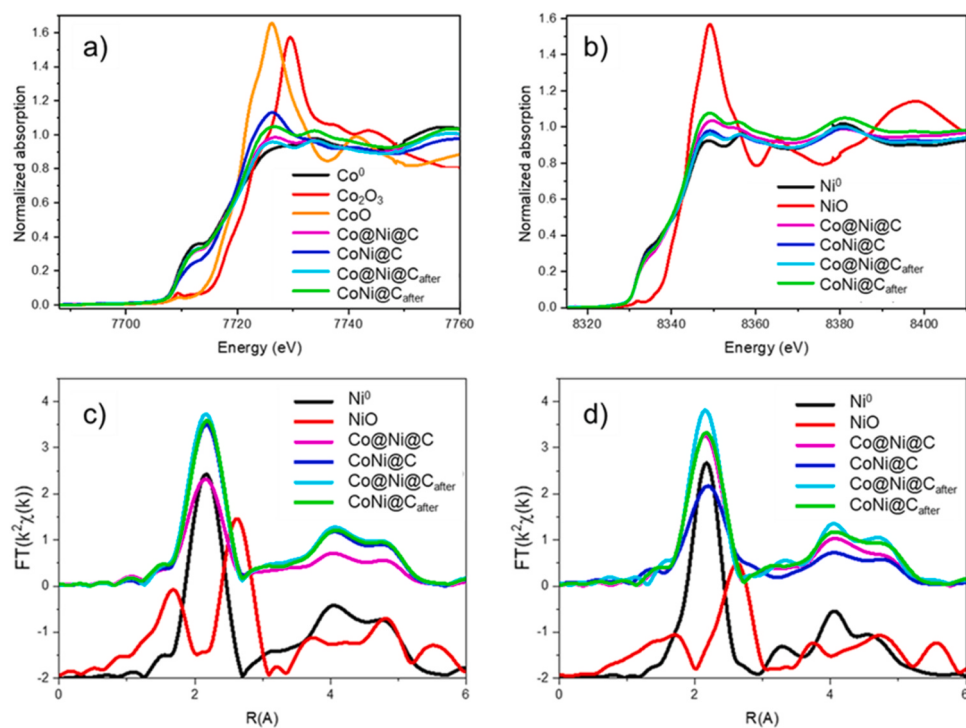


Fig. 8. (a, b) XANES spectra and (c, d) EXAFS Fourier transform at the Co-K and Ni-K edges of Co@Ni@C, CoNi@C, Co@Ni@C_{after} and Co@Ni@C_{after} together with reference materials of Co (Co⁰, Co₂O₃ and CoO) and Ni (Ni⁰ and NiO).

Table 2

Oxidation states of Co@Ni@C y CoNi@C, before and after catalytic conditions calculated by XANES.

Entry	Catalyst	Co ⁰ (%)	CoO (%)	Ni ⁰ (%)	NiO (%)
1	Co@Ni@C	89.5 (0.2)	10.5 (0.2)	81.2 (0.7)	18.8 (0.7)
2	Co@Ni@C _{after}	93.9 (0.4)	6.1 (0.4)	92.8 (0.2)	7.2 (0.2)
3	CoNi@C	67.8 (0.4)	32.2 (0.4)	91.0 (0.3)	9.0 (0.3)
4	CoNi@C _{after}	82.0 (0.7)	18.0 (0.7)	76.5 (1.4)	23.5 (1.4)

species present in this catalyst. Interestingly, above 460 °C a negative peak is observed, which is normally associated to the desorption of a gas. Since the change in the selectivity towards CO during catalysis occurs around a similar temperature (see Fig. 5a), this negative peak in the TPR profile could be a consequence of the structural transformation at this particular temperature. Above 400 °C, the desorption of an adsorbed gas on the MagNP surface is observed (probably H₂ strongly chemisorbed to the metal surface) [79,80] and may be related to the atomic restructuring that Co@Ni@C undergoes at this temperature. After losing the core-shell structure, H₂ previously adsorbed on the MagNP surface are desorbed [81]. When analyzing the TPR profile of Co@Ni@C_{after} (Fig. 9a), we observe a displacement of the Co and Ni reduction peaks to higher temperatures (244 and 319 °C) and a negligible contribution of the negative peak. Thus, the gas desorption is no longer observed after the afore mentioned intermediate state is reached during catalysis. The same trend was found for CoNi@C (Fig. 9b). Before catalysis the

reduction peaks of the oxidized species are observed (144 and 206 °C) together with a negative peak (413 °C). And after catalysis, the reduction peaks shift to higher temperatures and the negative contribution disappears, suggesting that there has been a change in the metallic distribution of the catalyst. Therefore, TPR provides us further information about the structural change observed, which is responsible for the high selectivity towards CO of the bimetallic catalysts. However, it is worth mentioning that this structural transformation does not generate two identical catalysts, since although both systems present high selectivity to CO even at low reaction temperatures, Co@Ni@C is much more active due to its higher heating capacity (74.2 vs. 51.3% at 53 mT, see Table 1).

TPD-CO₂ was performed to explore the affinity of the different catalysts towards CO₂ adsorption, which is crucial for CO₂ conversion. As can be seen in Fig. 10a, TPD-CO₂ of Co@Ni@C exhibits two weak signals at ca. 266 y 582 °C, and a more intense one at 362 °C. However, Co@Ni@C_{after} shows a significantly different profile, where only two signals can be observed at 276 and 623 °C, the latter being much more intense. This indicates that CO₂ desorption takes place at higher temperature in Co@Ni@C_{after} because CO₂ is strongly adsorbed to this catalyst surface. Likewise, TPD-CO₂ of CoNi@C (Fig. 10b) shows a main peak centered at 400 °C that switches to higher temperature after catalytic conditions (i.e. 595 °C). Similar to TPR measurements, the difference between TPD-CO₂ profiles before and after catalysis provides further evidence of the structural transformation observed under catalytic conditions. In addition, the higher affinity of Co@Ni@C_{after} and

Table 3

Number (N) and distances (R) between neighbouring atoms of Co@Ni@C y CoNi@C, before and after catalytic conditions calculated by EXAFS.

Entry	Catalyst	N	R					
			Co-M	Co-O	Ni-M	Ni-O	Co-M	Co-O
1	Co@Ni@C	10.08 (0.6)	-	6.81 (0.4)	5.81 (1.6)	2.492 (0.005)	-	2.489 (0.006)
2	Co@Ni@C _{after}	10.76 (0.7)	-	9.24 (0.5)	-	2.499 (0.007)	-	2.488 (0.005)
3	CoNi@C	9.17 (0.9)	5.31 (1.5)	8.81 (0.6)	-	2.496 (0.007)	2.035 (0.03)	2.493 (0.007)
4	CoNi@C _{after}	10.75 (0.8)	-	10.55 (0.8)	4.06 (1.6)	2.518 (0.004)	-	2.494 (0.005)

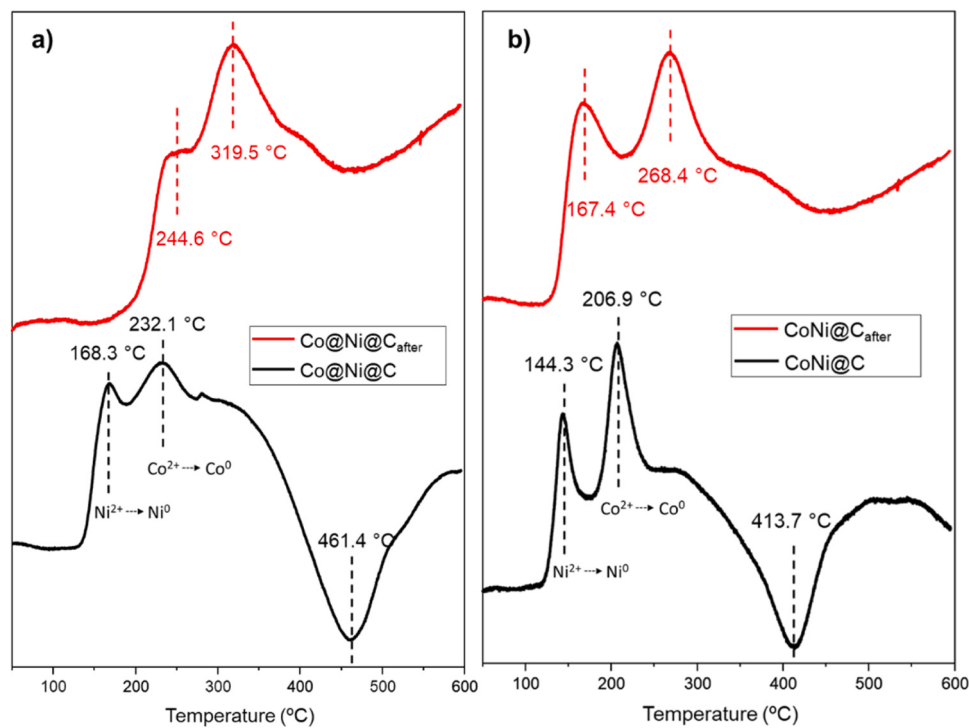


Fig. 9. TPR profiles of (a) $\text{Co}@\text{Ni}@\text{C}$ and (b) $\text{CoNi}@\text{C}$, before (black) and after (red) catalysis.

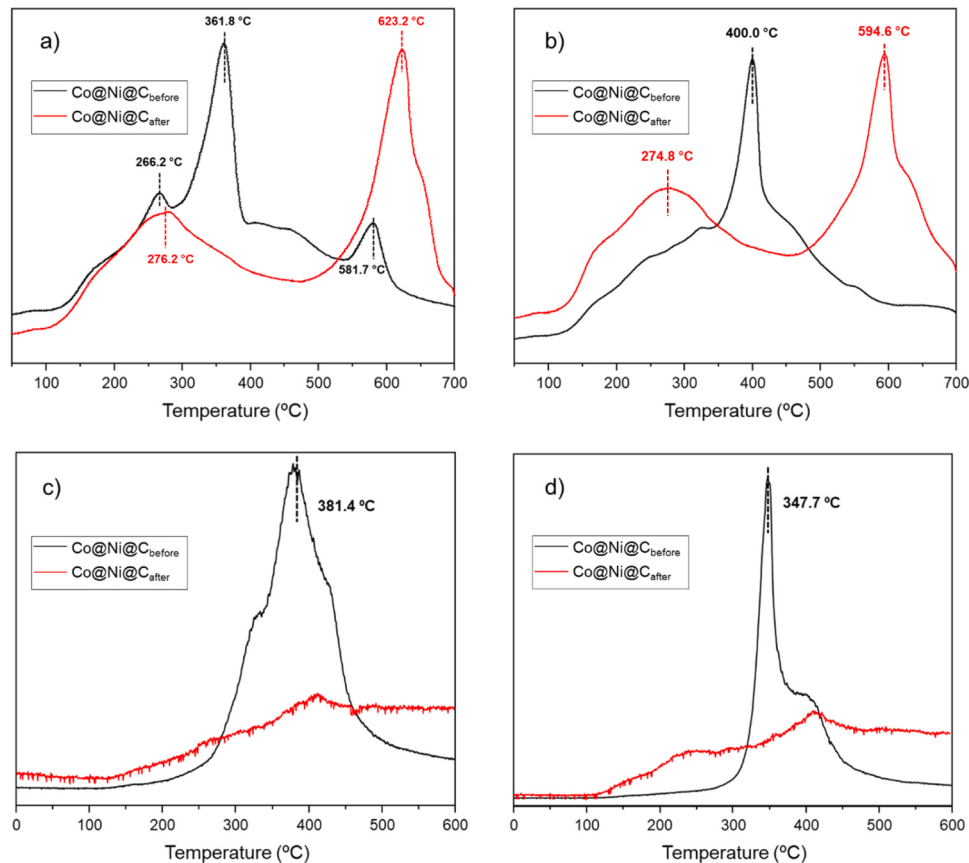


Fig. 10. (a, b) TPD-CO₂ and (c, d) TPD-CO profiles of $\text{Co}@\text{Ni}@\text{C}$ and $\text{CoNi}@\text{C}$, before (black) and after (red) catalysis.

CoNi@C_{after} for CO₂ than before they underwent the atomic restructuring, could explain the high catalytic activity observed in this reaction.

TPD-CO was also measured to determine the capacity to desorb CO of **Co@Ni@C** and **CoNi@C** before and after the structural change. As can be seen in Fig. 10c, TPD-CO of **Co@Ni@C** shows a peak at *ca.* 381 °C assigned to the desorption of CO by the catalyst at this temperature. However, the TPD-CO of the same catalyst after magnetic catalysis (**Co@Ni@C_{after}**) does not exhibit any noticeable desorption peak. This indicates that **Co@Ni@C_{after}** presents a high CO desorption capacity, and CO is probably desorbed during the signal stabilization time at room temperature, so its detection was not possible. The same trend was also observed for **CoNi@C** NPs (Fig. 10d), where before catalysis it is possible to observe a peak centered at *ca.* 348 °C, while after magnetic induction catalysis (**CoNi@C_{after}**) the TPD-CO spectrum does not show any perceptible desorption peak. Since for the formation of CH₄ it is necessary that the CO is more strongly adsorbed to the catalyst surface to be subsequently hydrogenated to methane,[28] the easy CO desorption observed in the catalysts after the structural transformation facilitates the RWGS reaction. The latter result, together with the high affinity of **Co@Ni@C_{after}** and **CoNi@C_{after}** for CO₂, justify their great activity in the selective formation of CO.

4. Conclusions

Magnetic core-shell **Co@Ni** NPs encapsulated in carbon (**Co@Ni@C**) have been simultaneously used as heating agent and catalyst in the magnetically induced hydrogenation of CO₂ to CO. First, it was concluded that the encapsulation process of the MagNPs by pyrolysis of the carbon-supported **Co@Ni** NPs needs to be carried out at a maximum temperature of 300 °C for two reasons: i) to preserve the core-shell structure of the MagNPs, since at higher temperatures they become alloy type MagNPs; and ii) to keep a large number of cracks/gaps in the carbon layer that favors the accessibility of the substrates to the active metal surface of the catalyst. Catalytic studies on the hydrogenation of CO₂ showed that at low field amplitudes **Co@Ni@C** produces mixtures of CO:CH₄, while at higher field amplitudes (*i.e.* 53 mT, T_{bulk} = 698 °C) it presents a high conversion and selectivity towards CO (74.2% conversion and 100% selectivity), being one of the most active catalysts reported to date (see SI section S10, Table S1). Interestingly, recycling and cyclability studies showed that after exposing **Co@Ni@C** to high magnetic fields (*i.e.* temperatures > 500 °C) it becomes fully selective to CO even at low field amplitudes (or temperatures). Microscopic (STEM-EDX), spectroscopic (XANES and EXAFS) and adsorption/desorption (TPR and TPD) studies have demonstrated that during magnetic catalysis, **Co@Ni@C** undergoes a structural transformation where surface Ni atoms diffuse towards the core of the nanoparticle, losing the core-shell structure and forming MagNPs that resembles an alloy type. However, the structure of this alloy is not homogeneous but could contain a gradient of concentration of cobalt into nickel. Similar behavior was observed for pure alloy type carbon-encapsulated CoNi NPs (**CoNi@C**), where a change in selectivity was also observed after exposing the catalyst to high field amplitudes. However, the activity of alloy-type **CoNi@C** NPs in CO₂ hydrogenation is much lower (51.3% conversion at 53 mT, 646 °C) due to their lower heating capacity. On the other hand, the monometallic Co catalyst (**Co@C**) is not only the least active catalyst (44.3% conversion at 53 mT, 635 °C), but also it does not suffer any change in the selectivity at high fields, producing CH₄:CO mixtures at low fields/temperatures. Thus, we can conclude that **Co@Ni@C** and **CoNi@C** catalysts undergo structural transformations during magnetic catalysis that make them highly selective in the hydrogenation of CO₂ to CO even at low fields/temperatures, and we propose that a gradient of concentration of one metal in the structure of the other be present. Such structure gradients with improved heating capacities and catalytic performances could be very interesting for future magnetically induced processes.

CRediT authorship contribution statement

Chaudret Bruno: Supervision, Writing – review & editing, Funding acquisition. **Martínez-Prieto Luis M:** Funding acquisition, Methodology, Project administration, Supervision, Writing – review & editing. **Mustieles Marine Irene:** Formal analysis, Investigation. **Marini Carlo:** Data curation, Formal analysis. **Cerezo-Navarrete Christian:** Formal analysis, Investigation, Writing – original draft.

Declaration of Competing Interest

The authors declare that they have no known competing financial interests or personal relationships that could have appeared to influence the work reported in this paper.

Data Availability

No data was used for the research described in the article.

Acknowledgements

The authors thank Instituto de Tecnología Química (ITQ), Instituto de Investigaciones Químicas (IIQ), Consejo Superior de Investigaciones Científicas (CSIC), Universitat Politècnica de València (UPV) and Universidad de Sevilla (US) for the facilities. We also thank the Electron Microscopy Service of the UPV for TEM analysis. The authors also acknowledge European Union's Horizon 2020 research and innovation program H2020-LC-SC3-2020 (LAURELIN; n°: 101022507), Agencia Estatal de Investigación, Ministerio de Ciencia e Innovación (PID2021-1260800A-I00, TED2021-132087A-I00 and RYC2020-0300031-I), Junta de Andalucía (ProyExcel_00706) and University of Seville (VI PP A. TALENTO; 2022/00000400) for financial support. We gratefully acknowledge Dr. Raf Roelant for his help with thermodynamic equilibrium calculations. C. Cerezo-Navarrete thanks Generalitat Valenciana Predoctoral Fellowship (GVA: ACIF/2019/076).

Appendix A. Supporting information

Supplementary data associated with this article can be found in the online version at doi:10.1016/j.apcatb.2024.123780.

References

- [1] W.M. Budzianowski, Implementing carbon capture, utilisation and storage in the circular economy, *Int. J. Glob. Warm.* 12 (2017) 272–296.
- [2] T. Sakakura, J.C. Choi, H. Yasuda, Transformation of carbon dioxide, *Chem. Rev.* 107 (2007) 2365–2387.
- [3] R.V. Gonçalves, L.L.R. Vono, R. Wojcieszak, C.S.B. Dias, H. Wender, E. Teixeira-Neto, L.M. Rossi, Selective hydrogenation of CO₂ into CO on a highly dispersed nickel catalyst obtained by magnetron sputtering deposition: a step towards liquid fuels, *Appl. Catal. B Environ.* 209 (2017) 240–246.
- [4] M.I. Alam, R. Cheula, G. Moroni, L. Nardi, M. Maestri, Mechanistic and multiscale aspects of thermo-catalytic CO₂ conversion to C1 products, *Catal. Sci. Technol.* 11 (2021) 6601–6629.
- [5] J.R. Rostrup-Nielsen, Production of synthesis gas, *Catal. Today* 18 (1993) 305–324.
- [6] Y.A. Daza, J.N. Kuhn, CO₂ conversion by reverse water gas shift catalysis: comparison of catalysts, mechanisms and their consequences for CO₂ conversion to liquid fuels, *RSC Adv.* 6 (2016) 49675–49691.
- [7] L. Peng, B. Jurca, A. Primo, A. Gordillo, V.I. Parvulescu, H. García, Co–Fe Clusters Supported on N-Doped Graphitic Carbon as Highly Selective Catalysts for Reverse Water Gas Shift Reaction, *ACS Sustain. Chem. Eng.* 9 (2021) 9264–9272.
- [8] P. Styring, E.A. Quadrrelli, K. Armstrong, Carbon Dioxide Utilisation: Closing the Carbon Cycle, First ed., Elsevier, Netherlands, 2014.
- [9] A.Y. Khodakov, W. Chu, P. Fongarland, Advances in the development of novel cobalt Fischer-Tropsch catalysts for synthesis of long-chain hydrocarbons and clean fuels, *Chem. Rev.* 107 (2007) 1692–1744.
- [10] M. González-Castaño, B. Dorneanu, H. Arellano-García, The reverse water gas shift reaction: a process systems engineering perspective, *React. Chem. Eng.* 6 (2021) 954.
- [11] Q.L. Tang, Q.J. Hong, Z.P. Liu, CO₂ fixation into methanol at Cu/ZrO₂ interface from first principles kinetic Monte Carlo, *J. Catal.* 263 (2009) 114–122.

[12] N. Ishito, K. Hara, K. Nakajima, A. Fukuoka, Selective synthesis of carbon monoxide via formates in reverse water-gas shift reaction over alumina-supported gold catalyst, *J. Energy Chem.* 25 (2016) 306–310.

[13] L. Liu, S. Das, T. Chen, N. Dewangan, J. Ashok, S. Xi, A. Borgna, Z. Li, S. Kawi, Low temperature catalytic reverse water-gas shift reaction over perovskite catalysts in DBD plasma, *Appl. Catal. B Environ.* 265 (2020) 118573.

[14] D.J. Pettigrew, D.L. Trimm, N.W. Cant, The effects of rare earth oxides on the reverse water-gas shift reaction on palladium/alumina, *Catal. Lett.* 28 (1994) 313–319.

[15] N.C. Nelson, L. Chen, D. Meira, L. Kovarik, J. Szanyi, In situ dispersion of palladium on TiO_2 during reverse water-gas shift reaction: formation of atomically dispersed palladium, *Angew. Chem. Int. Ed.* 59 (2020) 17657–17663.

[16] X. Chen, X. Su, H. Duan, B. Liang, Y. Huang, T. Zhang, Catalytic performance of the Pt/TiO_2 catalysts in reverse water gas shift reaction: controlled product selectivity and a mechanism study, *Catal. Today* 281 (2017) 312–318.

[17] Z. Zhao, M. Wang, P. Ma, Y. Zheng, J. Chen, H. Li, X. Zhang, K. Zheng, Q. Kuang, Z. X. Xie, Atomically dispersed Pt/CeO_2 catalyst with superior CO selectivity in reverse water gas shift reaction, *Appl. Catal. B Environ.* 291 (2021) 120101.

[18] D.H. Kim, S.W. Han, H.S. Yoon, Y.D. Kim, Reverse water gas shift reaction catalyzed by Fe nanoparticles with high catalytic activity and stability, *J. Ind. Eng. Chem.* 23 (2015) 67–71.

[19] S. Sengupta, A. Jha, P. Shende, R. Maskara, A.K. Das, Catalytic performance of Co and Ni doped Fe-based catalysts for the hydrogenation of CO_2 to CO via reverse water-gas shift reaction, *J. Environ. Chem. Eng.* 7 (2019) 102911.

[20] R. Mutschler, E. Moioli, W. Luo, N. Gallandat, A. Züttel, CO_2 hydrogenation reaction over pristine Fe, Co, Ni, Cu and Al_2O_3 supported Ru: Comparison and determination of the activation energies, *J. Catal.* 366 (2018) 139–149.

[21] M.M. Millet, G. Algara-Siller, S. Wrabetz, A. Mazheika, F. Girsdis, D. Teschner, F. Seitz, A. Tarasov, S.V. Levchenko, R. Schlägl, E. Frei, Ni single atom catalysts for CO_2 activation, *J. Am. Chem. Soc.* 141 (2019) 2451–2461.

[22] X. Zhang, X. Zhu, L. Lin, S. Yao, M. Zhang, X. Liu, X. Wang, Y.W. Li, C. Shi, D. Ma, Highly dispersed copper over $\beta\text{-Mo}_2\text{C}$ as an efficient and stable catalyst for the reverse water gas shift (RWGS) reaction, *ACS Catal.* 7 (2017) 912–918.

[23] S.C. Yang, S.H. Pang, T.P. Sulmonetti, W.N. Su, J.F. Lee, B.J. Hwang, C.W. Jones, Synergy between ceria oxygen vacancies and Cu nanoparticles facilitates the catalytic conversion of CO_2 to CO under mild conditions, *ACS Catal.* 8 (2018) 12056–12066.

[24] A.G. Kharaji, A. Shariati, Selectivity and performance of $\text{Ni-Mo}/\gamma\text{-Al}_2\text{O}_3$ catalyst for methanol production with reverse water gas shift (RWGS) reaction, *J. Am. Sci. 8* (2012) 265–270.

[25] J. Ye, Q. Ge, C.J. Liu, Effect of PdIn bimetallic particle formation on CO_2 reduction over the $\text{Pd-In}/\text{SiO}_2$ catalyst, *Chem. Eng. Sci.* 135 (2015) 193–201.

[26] Q. Zhang, L. Pastor-Pérez, W. Jin, S. Gu, T.R. Reina, Understanding the promoter effect of Cu and Cs over highly effective $\beta\text{-Mo}_2\text{C}$ catalysts for the reverse water-gas shift reaction, *Appl. Catal. B Environ.* 244 (2019) 889–898.

[27] T.S. Galhardo, A.H. Braga, B.H. Arpini, J. Szanyi, R.V. Gonçalves, B.F. Zornio, C. R. Miranda, L.M. Rossi, Optimizing active sites for high CO selectivity during CO_2 hydrogenation over supported nickel catalysts, *J. Am. Chem. Soc.* 143 (2021) 4268–4280.

[28] B.H. Arpini, A.H. Braga, L.R. Borges, P. Vidinha, R.V. Gonçalves, J. Szanyi, L. M. Rossi, Tuning CO_2 hydrogenation selectivity by N-doped carbon coating over nickel nanoparticles supported on SiO_2 , *ACS Sustain. Chem. Eng.* 10 (2022) 2331–2342.

[29] G. Benkowsky, *Induction Heating*, Verlag Technik, Berlin, 1990.

[30] E.C. Abenajar, S. Wickramasinghe, J. Bas-Concepcion, A.C.S. Samia, Structural effects on the magnetic hyperthermia properties of iron oxide nanoparticles, *Prog. Nat. Sci. Mater. Int.* 26 (2016) 440–448.

[31] W. Wang, G. Tuci, C. Duong-Viet, Y. Liu, A. Rossin, L. Luconi, J.M. Nhut, L. Nguyen-Dinh, C. Pham-Huu, G. Giambastiani, Induction heating: an enabling technology for the heat management in catalytic processes, *ACS Catal.* 9 (2019) 7921–7935.

[32] J.M. Asensio, A.B. Miguel, P. Fazzini, P.W.N.M. van Leeuwen, B. Chaudret, Hydrodeoxygenation using magnetic induction: high-temperature heterogeneous catalysis in solution, *Angew. Chem. Int. Ed.* 58 (2019) 11306–11310.

[33] S. Gyergyek, A. Kocjan, M. Grile, B. Likozar, B. Hočevar, D. Makovec, A hierarchical Ru-bearing alumina/magnetic iron-oxide composite for the magnetically heated hydrogenation of furfural, *Green. Chem.* 22 (2020) 5978–5983.

[34] H. Kreissl, J. Jin, S.-H. Lin, D. Schüette, S. Störte, N. Levin, B. Chaudret, A. J. Vorholt, A. Bordet, W. Leitner, Commercial $\text{Cu}_2\text{Cr}_2\text{O}_5$ decorated with iron carbide nanoparticles as a multifunctional catalyst for magnetically induced continuous-flow hydrogenation of aromatic ketones, *Angew. Chem. Int. Ed.* 60 (2021) 26639–26646.

[35] C. Cerezo-Navarrete, I.M. Marin, H. García-Miquel, A. Corma, B. Chaudret, L. M. Martínez-Prieto, Magnetically induced catalytic reduction of biomass-derived oxygenated compounds in water, *ACS Catal.* 12 (2022) 8462–8475.

[36] Y. Liu, P. Gao, N. Cherkasov, E.V. Rebrov, Direct amide synthesis over core-shell $\text{TiO}_2@\text{NiFe}_2\text{O}_4$ catalysts in a continuous flow radiofrequency-heated reactor, *RSC Adv.* 6 (2016) 100997–101007.

[37] Y. Liu, N. Cherkasov, P. Gao, J. Fernández, M.R. Lees, E.V. Rebrov, The enhancement of direct amide synthesis reaction rate over $\text{TiO}_2@\text{SiO}_2@\text{NiFe}_2\text{O}_4$ magnetic catalysts in the continuous flow under radiofrequency heating, *J. Catal.* 355 (2017) 120–130.

[38] Y. Liu, E.V. Rebrov, Direct amide synthesis over composite magnetic catalysts in a continuous flow, *React., Catal.* 11 (2021) 146.

[39] C. Niether, S. Faure, A. Bordet, J. Deseure, M. Chatenet, J. Carrey, B. Chaudret, A. Rouet, Improved water electrolysis using magnetic heating of FeC-Ni core–shell nanoparticles, *Nat. Energy* 3 (2018) 476–483.

[40] H.B. Zheng, H.H. Chen, Y.L. Wang, P.Z. Gao, X.P. Liu, E.V. Rebrov, Fabrication of magnetic superstructure $\text{NiFe}_2\text{O}_4@\text{MOF-74}$ and its derivative for electrocatalytic hydrogen evolution with AC magnetic field, *ACS Appl. Mater. Interfaces* 12 (2020) 45987–45996.

[41] I. Mustiéles Marin, D. De Masi, L.M. Lacroix, P.F. Fazzini, P.W.N.M. van Leeuwen, J.M. Asensio, B. Chaudret, Hydrodeoxygenation and hydrogenolysis of biomass-based materials using FeNi catalysts and magnetic induction, *Green. Chem.* 23 (2021) 2025–2036.

[42] A. Meffre, B. Mehdaoui, V. Connard, J. Carrey, P.F. Fazzini, S. Lachaize, M. Respaud, B. Chaudret, Complex nano-objects displaying both magnetic and catalytic properties: A proof of concept for magnetically induced heterogeneous catalysis, *Nano Lett.* 15 (2015) 3241–3248.

[43] A. Bordet, L.M. Lacroix, P.F. Fazzini, J. Carrey, K. Soulantica, B. Chaudret, Magnetically induced continuous CO_2 hydrogenation using composite iron carbide nanoparticles of exceptionally high heating power, *Angew. Chem. Int. Ed.* 55 (2016) 15894–15898.

[44] A. Bordet, J. Manuel Asensio, K. Soulantica, B. Chaudret, A. Bordet, J.M. Asensio, K. Soulantica, B. Chaudret, Enhancement of carbon oxides hydrogenation on iron-based nanoparticles by in-situ water removal, *ChemCatChem* 10 (2018) 4047–4051.

[45] S.S. Kale, J.M. Asensio, M. Estrader, M. Werner, A. Bordet, D. Yi, J. Marbaix, P. F. Fazzini, K. Soulantica, B. Chaudret, Iron carbide or iron carbide/cobalt nanoparticles for magnetically-induced CO_2 hydrogenation over Ni/SiAlO_x catalysts, *Catal. Sci. Technol.* 9 (2019) 2601–2607.

[46] D. De Masi, J.M. Asensio, P.F. Fazzini, L.M. Lacroix, B. Chaudret, Engineering iron–nickel nanoparticles for magnetically induced CO_2 methanation in continuous flow, *Angew. Chem. Int. Ed.* 59 (2020) 6187–6191.

[47] M.G. Vinum, M.R. Almind, J.S. Engbæk, S.B. Vendelbo, M.F. Hansen, C. Frandsen, J. Bendix, P.M. Mortensen, Dual-function cobalt–nickel nanoparticles tailored for high-temperature induction-heated steam methane reforming, *Angew. Chem. Int. Ed.* 57 (2018) 10569–10573.

[48] F. Varsano, M. Bellusci, A. La Barbera, M. Petrecca, M. Albino, C. Sangregorio, Dry reforming of methane powered by magnetic induction, *Int. J. Hydrog. Energy* 44 (2019) 21037–21044.

[49] M.R. Almind, M.G. Vinum, S.T. Wismann, M.F. Hansen, S.B. Vendelbo, J. S. Engbaek, P.M. Mortensen, I. Chorkendorff, C. Frandsen, J.S. Engbæk, P. M. Mortensen, I. Chorkendorff, C. Frandsen, Optimized CoNi nanoparticle composition for curie-temperature-controlled induction-heated catalysis, *ACS Appl. Nano Mater.* 4 (2021) 11537–11544.

[50] J. Marbaix, N. Mille, L.-M. Lacroix, J.M. Asensio, P.-F. Fazzini, K. Soulantica, J. Carrey, B. Chaudret, Tuning the composition of FeCo nanoparticle heating agents for magnetically induced catalysis, *ACS Appl. Nano Mater.* 3 (2020) 3767–3778.

[51] J.P. Fortin, C. Wilhelm, J. Servais, C. Ménager, J.C. Bacri, F. Gazeau, Size-sorted anionic iron oxide nanomagnets as colloidal mediators for magnetic hyperthermia, *J. Am. Chem. Soc.* 129 (2007) 2628–2635.

[52] B. Mehdaoui, A. Meffre, J. Carrey, S. Lachaize, L.M. Lacroix, M. Gougeon, B. Chaudret, M. Respaud, Optimal size of nanoparticles for magnetic hyperthermia: a combined theoretical and experimental study, *Adv. Funct. Mater.* 21 (2011) 4573–4581.

[53] M.A. Newton, Dynamic adsorbate/reaction induced structural change of supported metal nanoparticles: heterogeneous catalysis and beyond, *Chem. Soc. Rev.* 37 (2008) 2644–2657.

[54] L. Liu, A. Corma, Structural transformations of solid electrocatalysts and photocatalysts, *Nat. Rev. Chem.* 5 (2021) 256–276.

[55] N.E. Tsakoumis, M. Ronning, Ø. Borg, E. Rytter, A. Holmen, Deactivation of cobalt based Fischer–Tropsch catalysts: a review, *Catal. Today* 154 (2010) 162–182.

[56] G. Malta, S.A. Kondrat, S.J. Freakley, C.J. Davies, S. Dawson, X. Liu, L. Lu, K. Dymkowski, F. Fernandez-Alonso, S. Mukhopadhyay, E.K. Gibson, P.P. Wells, S. F. Parker, C.J. Kiely, G.J. Hutchings, Deactivation of a single-site gold-on-carbon acetylene hydrochlorination catalyst: an X-ray absorption and inelastic neutron scattering study, *ACS Catal.* 8 (2018) 8493–8505.

[57] J.C. Matsubu, S. Zhang, L. DeRita, N.S. Marinkovic, J.G. Chen, G.W. Graham, X. Pan, P. Christopher, Adsorbate-mediated strong metal–support interactions in oxide-supported Rh catalysts, *Nat. Chem.* 9 (2016) 120–127.

[58] H.L. Xin, S. Alayoglu, R. Tao, A. Genc, C.M. Wang, L. Kovarik, E.A. Stach, L. W. Wang, M. Salmeron, G.A. Somorjai, H. Zheng, Revealing the atomic restructuring of Pt-Co nanoparticles, *Nano Lett.* 14 (2014) 3203–3207.

[59] B. Zugic, L. Wang, C. Heine, D.N. Zakharov, B.A.J. Lechner, E.A. Stach, J. Biener, M. Salmeron, R.J. Madix, C.M. Friend, Dynamic restructuring drives catalytic activity on nanoporous gold–silver alloy catalysts, *Nat. Mater.* 16 (2016) 558–564.

[60] L. Liu, A. Corma, Evolution of isolated atoms and clusters in catalysis, *Trends Chem.* 2 (2020) 383–400.

[61] J.S. Bradley, E.W. Hill, B. Chaudret, A. Duteil, Surface chemistry on colloidal metals. Reversible adsorbate-induced surface composition changes in colloidal palladium–copper alloys, *Langmuir* 11 (1995) 693–695.

[62] F. Tao, M.E. Grass, Y. Zhang, D.R. Butcher, J.R. Renzas, Z. Liu, J.Y. Chung, B. S. Mun, M. Salmeron, G.A. Somorjai, Reaction-driven restructuring of Rh–Pd and Pt–Pd core–shell nanoparticles, *Science* 322 (2008) 932–934.

[63] X. Zhang, S. Han, B. Zhu, G. Zhang, X. Li, Y. Gao, Z. Wu, B. Yang, Y. Liu, W. Baaziz, O. Ersen, M. Gu, J.T. Miller, W. Liu, Reversible loss of core–shell structure for Ni–Au bimetallic nanoparticles during CO_2 hydrogenation, *Nat. Catal.* 3 (2020) 411–417.

[64] L. Zou, C. Yang, Y. Lei, D. Zakharov, J.M.K. Wiezorek, D. Su, Q. Yin, J. Li, Z. Liu, E. A. Stach, J.C. Yang, L. Qi, G. Wang, G. Zhou, Dislocation nucleation facilitated by atomic segregation, *Nat. Mater.* 17 (2017) 56–63.

[65] N.J. Divins, I. Angurell, C. Escudero, V. Pérez-Dieste, J. Llorca, Influence of the support on surface rearrangements of bimetallic nanoparticles in real catalysts, *Science* 346 (2014) 620–623.

[66] L.M. Martínez-Prieto, J. Marbaix, J.M. Asensio, C. Cerezo-Navarrete, P.F. Fazzini, K. Soulantica, B. Chaudret, A. Corma, Ultrastable magnetic nanoparticles encapsulated in carbon for magnetically induced catalysis, *ACS Appl. Nano Mater.* 2020 (2020) 7076–7087.

[67] J. Deng, P. Ren, D. Deng, X. Bao, J. Deng, P. Ren, D. Deng, X. Bao, Z. Zhang, Y. Wang, W. Yuan, Enhanced electron penetration through an ultrathin graphene layer for highly efficient catalysis of the hydrogen evolution reaction, *Angew. Chem. Int. Ed.* 54 (2015) 2100–2104.

[68] L.M. Martínez-Prieto, M. Puche, C. Cerezo-Navarrete, B. Chaudret, Uniform Ru nanoparticles on N-doped graphene for selective hydrogenation of fatty acids to alcohols, *J. Catal.* 377 (2019) 429–437.

[69] A.C. Ferrari, Raman spectroscopy of graphene and graphite: Disorder, electron-phonon coupling, doping and nonadiabatic effects, *Solid State Commun.* 143 (2007) 47–57.

[70] S.L. Saville, B. Qi, J. Baker, R. Stone, R.E. Camley, K.L. Livesey, L. Ye, T. M. Crawford, O. Thompson, The formation of linear aggregates in magnetic hyperthermia: Implications on specific absorption rate and magnetic anisotropy, *J. Colloid Interface Sci.* 424 (2014) 141–151.

[71] Z.J. Díaz-Puerto, Á. Raya-Barón, P.W.N.M. van Leeuwen, J.M. Asensio, B. Chaudret, Determination of the surface temperature of magnetically heated nanoparticles using a catalytic approach, *Nanoscale* 13 (2021) 12438–12442.

[72] B. Rivas-Murias, V. Salgueirín, Thermodynamic CoO-Co₃O₄ crossover using Raman spectroscopy in magnetic octahedron-shaped nanocrystals, *J. Raman Spectrosc.* 48 (2017) 837–841.

[73] M. Wu, S. Chen, A. Soomro, S. Ma, M. Zhu, X. Hua, W. Xiang, Investigation of synergistic effects and high performance of La-Co composite oxides for toluene catalytic oxidation at low temperature, *Environ. Sci. Pollut. Res.* 26 (2019) 12123.

[74] The formation of CH₄ species due to the carbide hydrogenation was not observed during an online H₂ temperature programmed reduction (H₂-TPR) performed in a continuous flow reactor connected to a mass spectrometer (MS). The mass signals corresponding to *m/z* = 16, 15 and 14 were not detected in this online experiment, which points to the absence of Ni surface carbides on Co@Ni@C_{after}.

[75] The catalytic performance of Co@Ni@C_{after} after a regeneration treatment (heated at 500 °C under a H₂ flow over 5h to facilitate the desorption of possible pollutants or the formation of CH₄ due to the hydrogenation of Ni-C species) showed 100% selectivity towards CO even at low magnetic fields. The latter result indicates the absence of surface species which can be responsible of the change in the selectivity.

[76] C. Garnero, M. Lepesant, C. Garcia-Marcelot, Y. Shin, C. Meny, P. Farger, B. Warot-Fonrose, R. Arenal, G. Viau, K. Soulantica, P. Fau, P. Poveda, L.-M. Lacroix, B. Chaudret, Chemical ordering in bimetallic FeCo nanoparticles: from a direct chemical synthesis to application as efficient high-frequency magnetic material, *Nano Lett.* 19 (2019) 1379–1386.

[77] L. Liu, F. Gao, P. Concepción, A. Corma, A new strategy to transform mono and bimetallic non-noble metal nanoparticles into highly active and chemoselective hydrogenation catalysts, *J. Catal.* 350 (2017) 218–225.

[78] C. Hernández Mejía, J.E.S. Van Der Hoeven, P.E. De Jongh, K.P. De Jong, Cobalt-nickel nanoparticles supported on reducible oxides as fischer-tropsch catalysts, *ACS Catal.* 10 (2020) 7343–7354.

[79] H. Li, J. Ren, X. Qin, Z. Qin, J. Lin, Z. Li, Ni/SBA-15 catalysts for CO methanation: effects of V, Ce, and Zr promoters, *RSC Adv.* 5 (2015) 96504–96517.

[80] Y. Ma, J. Liu, M. Chu, J. Yue, Y. Cui, G. Xu, Cooperation between active metal and basic support in Ni-based catalyst for low-temperature CO₂ methanation, *Catal. Lett.* 150 (2020) 1418–1426.

[81] After analyzing by GC-MS the desorbed gas at ~ 400 °C, it was confirmed that it was H₂.